Measurements of Inelastic Energy Loss in Atomic Collisions of Al^+, P^+, S^+, Cl^+, Ar^+, K^+, and Mn^+ on Argon at keV Energies and Large Scattering Angles

B. Fastrup, G. Hermann, and K. J. Smith
Institute of Physics, University of Aarhus, 8000 Aarhus C, Denmark
(Received 6 November 1970)

The inelastic energy-loss distribution Q has been measured for single large-angle collisions between argon atoms and incident projectile ions with atomic numbers Z_1 ranging from 13 to 25. The data are obtained by measuring the energy and scattering angle of the scattered incident particle. This method provides well-resolved Q spectra, being almost undisturbed by thermal target motion. In all cases studied, the Q value exhibits a sudden change and a triple-peaked structure in a narrow range of distance of closest approach r_0. The location of the three peaks Q_{I}, Q_{II}, and Q_{III} varies with r_0, but their energy separations remain independent of r_0. For the heteronuclear collisions reported here, the values of the Q-peak separations suggest that Q_{II} and Q_{III} correspond to the production of one and two $L_{2,3}$ vacancies, respectively, in one of the colliding particles, viz., the one with the lower atomic number. This is further supported by studies of Auger electrons emitted in the collisions.

I. INTRODUCTION

In the last few years, measurements of inelastic energy loss in violent heavy-ion–atom collisions, where inner shells begin to interpenetrate, have become a field of great interest. These studies, combined with spectroscopic investigations of the resulting excitations, have given valuable insight into the dynamics of many-electron excitations in heavy atoms.

The original coincidence measurements by Afrosimov *et al.*[1] and Kessel and co-workers[2] on inelastic energy loss in Ar^+-Ar collisions revealed a triple-peaked Q structure in a narrow range of distances of closest approach around $r_0 = 0.24$ Å. The Ar^+-Ar data and the more recent Ne^+-Ne data in Kessel *et al.*,[3] where similar peculiar structures were seen around $r_0 = 0.06$ Å, were analyzed by Fano and Lichten[4] and by Lichten[5] within the framework of the molecular-orbital (MO) model for homonuclear systems. The triple-peaked structure in the Ar^+-Ar collisions was explained as being the result of the promotion of one or two $L_{2,3}$ electrons to certain excited states in the colliding particles. In the MO model, which is essentially based on an adiabatic MO calculation for the H_2^+ system at various interatomic separation distances, Fano and Lichten assumed that dynamic transitions (so-called diabatic transitions) could occur during the collision. In the pure adiabatic case, these transitions are otherwise forbidden by the noncrossing rule of molecular orbitals.

Recently, very precise data by Afrosimov *et al.*[6] on Ar^+-Ar collisions at 25 keV and 16° scattering angle have shown that the energy separations between the three Q peaks ($\bar{Q}_{\mathrm{II}} - \bar{Q}_{\mathrm{I}}$ and $\bar{Q}_{\mathrm{III}} - \bar{Q}_{\mathrm{II}}$) nicely match the binding energy of an $L_{2,3}$ electron in argon. These data, which are in good agreement with the data reported here, are consistent with the MO model, wherein a $4f\sigma_u$ orbital crosses several orbitals, and thereby one or two electrons are promoted from the atomic $L_{2,3}$ subshells to excited states. This leaves either one or both colliding particles with an $L_{2,3}$ vacancy. The range of r_0 values, where the MO promotions occur, seems to shift slightly toward higher r_0 values with increasing velocity of the incident ions.

Besides inner-shell excitations, the collisions produce very complex excitations in the outer shell (up to a couple of hundred eV of excitation energy). These excitations, which are far above the ionization threshold, decay through fast autoionization transitions, causing the ejection of one or more M electrons. By statistical reasoning, Russek and Meli[7] estimated the final charge-state distributions of the colliding particles, and good over-all agreement with experimental data was achieved.[2] The coincidence measurements on Ar^+-Ar by Kessel and co-workers[2] showed that the charge states of the two scattered particles are roughly uncorrelated except for collisions where the excitation is of type Q_{II}, in which case a special correlation exists.

Other Q measurements on heavy-ion collisions with Ar as one of the collision partners have been performed by Snoek *et al.*[8] (Ar^+-Cu), Kessel[9] (Ne^+-Ar), Bingham[10] (O^+-Ar), Afrosimov *et al.*[11] (Ne^+-Ar), and Knystautas *et al.*[12] (N^+-Ar). By means of recoil-scattering cross-section data, Loftager and Hermann[13] have indirectly studied Q structure in P^+, Cl^+, and K^+-Ar collisions.

Inner-shell vacancies in argon preferentially decay by Auger transitions, where one M electron fills the vacancy and another M electron is ejected with a well-defined kinetic energy. X-ray emission is not probable because the fluoresence yield is only of the order of 1 part in 10^3 for the argon L

shell.[14] By a noncoincidence technique, Rudd *et al.*,[15] Snoek *et al.*,[16] and Ogurtsov *et al.*[17] studied *LMM* Auger electrons in Ar^+-Ar collisions and found a predominant electron group with energies around 170–190 eV. The broad unresolved distribution of electrons [half-width at half-maximum (HWHM) $\simeq$ 30 eV] probably consists of many closely spaced $L_{2,3}$ *MM* Auger lines corresponding to the many different decay channels in the highly excited (ionized) scattered particles. In a noncoincidence experiment, the angle is not specified between the velocity vectors of the emitted electron and that of the moving atom from which it is emitted. This causes a Doppler-shift[15] broadening which may obscure structures in the measured electron spectra.

Ordinarily, one electron is ejected in an Auger process. Carlson and Krause,[18] however, have reported the possibility of having the ejection of more than one electron in an Auger process.

Recent electron studies in Ar^+-Ar collisions by Ogurtsov *et al.*[19] have indicated the existence of L_1MM Auger transitions resulting from the production of L_1 vacancies. According to the MO model, these vacancies are expected to be produced at r_0 values substantially smaller than 0.24 Å, where the $L_{2,3}$ vacancies are in fact produced. Experimental studies by Kessel and Everhart[2] have clearly demonstrated a sudden step in the mean Q at $r_0 \simeq 0.15$ Å, possibly due to crossings of MO's producing L_1 vacancies. Experimental studies of Auger electrons in coincidence with the scattered ions in Ar^+-Ar collisions (Thomson *et al.*[20]) and in P^+-Ar collisions[21] have strongly and directly supported the general results of the Q measurements.

Although the MO model was established for homonuclear systems only, we found it important to extend the experimental studies to include a systematic investigation of heteronuclear collisions with argon to see if these systems show any similarities with the Ar^+-Ar system. Our preliminary results have been described.[22] The data include collision studies of Al^+, P^+, S^+, Cl^+, Ar^+, K^+, and Mn^+ on Ar. To obtain well-resolved Q spectra, we chose an improved measuring technique where the energy distribution and the charge states of the scattered incident particles are measured at different scattering angles and energies of the incident particles. This method is referred to as the scattered-particle method.

In all cases studied, triple-peaked Q structures are found in a narrow range of r_0 values. Outside that range, the Q distributions are single-peaked. In the P^+-Ar case, both the scattered and the recoil particles are studied.

The structure of the electron spectra is also studied here. Utilizing the Doppler-shift effect, it is possible to decide which of the two colliding particles has ejected the Auger electrons. The general results are in good agreement with the conclusions drawn from the analysis of the Q structure.

II. KINEMATICAL CONSIDERATIONS

The inelastic energy loss

$$Q = E_0 - (E_1 + E_2), \tag{1}$$

where E_0, E_1, and E_2 are the kinetic energies of the incident and the scattered and recoil particles, respectively, may be obtained in at least three different ways: The early Q studies were carried out by the recoil-particle method, i.e., by measuring the energy and the scattering angle of the recoils. In fact, the earliest such measurements by Morgan and Everhart[23] of Ar^+-Ar collisions revealed structures in the Q spectra which were later known[1,2] as the triple structures. Another method of measuring Q values is to determine the angles of the scattered and the recoil particles in coincidence.[1,2] This widely used method has recently been improved by Afrosimov *et al.*,[6] who did not only make coincidence measurements, but also determined the energies of the two scattered particles. This modified coincidence method gives excellent results, but is time consuming. Still another method, the scattered-particle method, where the energy and the angle of the scattered incident particles alone are measured, is adopted here. A discussion and a comparison of these methods are given below.

The scattered-particle method is first considered. By means of Eq. (1) and momentum conservation in the collision, we obtain

$$Q = 2\gamma(E_0E_1)^{1/2}\cos\theta + (1-\gamma)E_0 - (1+\gamma)E_1, \tag{2}$$

where $\gamma = M_1/M_2$ is the mass ratio between the incident particle and the target particle, and θ is the scattering angle of the scattered incident particles.

For the recoil-particle method, the corresponding equation is

$$Q = 2(E_0E_2/\gamma)^{1/2}\cos\phi - (1+1/\gamma)E_2, \tag{3}$$

where ϕ is the scattering angle of the recoils.

Below are given some of the reasons for preferring the scattered-particle method over the recoil-particle method.

(i) For a given collision, the scattered incident particles yield a better intensity per unit solid angle than do the recoils.

(ii) The measured spectra obtained for various charge states of the scattered incident particles are well separated, whereas they may overlap for the recoils, particularly in the triple-peaked Q region.

(iii) Transformation of the recoil scattering angle ϕ in the laboratory system (see Fig. 1) to the c.m. angle ϑ depends significantly on the Q value of the collision,[13] while the corresponding transformation of the scattering angle θ is almost unaffected

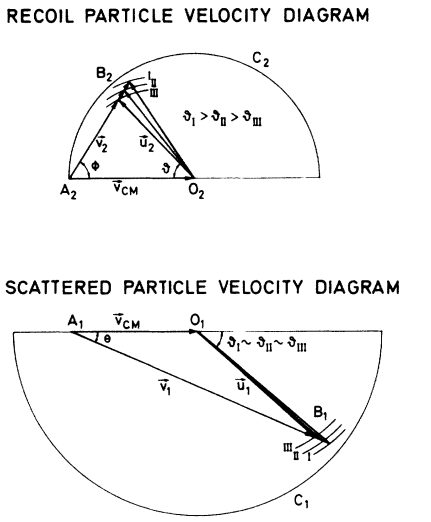

FIG. 1. Velocity diagram for recoils and scattered incident particles in the $M_1 < M_2$ case. $\vec{v}_1$ and $\vec{v}_2$ are velocity vectors in the laboratory system of the scattered incident particle and the recoil particle, respectively; $\vec{u}_1$ and $\vec{u}_2$ are the velocity vectors in the c.m. system for the same particles, and $\vec{v}_{c.m.}$ is the velocity of the c.m. On the upper figure, the triangle $A_2 B_2 O_2$ shows the construction of the c. m. scattering angle φ for a collision with specified ϕ and $v_{c.m.}$. ϑ_I, ϑ_{II}, and ϑ_{III} correspond to the three Q values Q_I, Q_{II}, and Q_{III}, respectively. In the elastic case (not shown), B_2 falls on the circular arc C_2 ($u_2 = v_{c.m.}$). The lower figure shows the same construction for scattered incident particles. It is seen that for recoils, the influence of Q on ϑ can be appreciable, whereas it is negligible for the scattered incident particles.

by Q. To illustrate the effect on the recoils, let us consider a 20-keV P^+-Ar collision with a 77° recoil angle. This collision has a triple-peaked Q structure, where the three $\bar{Q}$ values are $\bar{Q}_I = 100$ eV, $\bar{Q}_{II} = 250$ eV, and $\bar{Q}_{III} = 400$ eV. The corresponding c. m. scattering angles ϑ are 24°50′, 22°49′, and 20°11′. Since the differential scattering cross section depends strongly on the c. m. scattering angle ϑ, it also depends on Q. An additional complication is that the transformation of the solid angle of the recoil particles from the laboratory system to the c. m. system depends on the variation of Q with ϑ. All these problems make the analysis of the energy spectra of recoils very complicated.

(iv) The thermal motion of the target atoms affects the widths of the "lines" in the energy spectra of both the scattered and the recoil particles. A detailed analysis given in the Appendix shows that the thermal target motion broadens the lines in the recoil-energy spectra considerably more than the lines in the energy spectra of the scattered particles.

In cases where the lines are closely spaced, this broadening effect may wash out structure in the recoil-energy spectra, whereas structure in the energy spectra of the scattered incident particles will be better resolved.

It can also be shown (see Appendix) that the thermal target motion affects the linewidths in the Q spectra obtained by the recoil-particle method and the coincidence method to the same extent. This is partly the reason why coincidence measurements of Kr^+-Kr collisions[24] revealed no triple-peaked Q structures in the range of r_0 values studied. The modified coincidence technique of Afrosimov *et al.*[6] offers the same advantages as does the scattered-particle method with the additional information of the coincidence data.

III. APPARATUS

The incident ion beam is supplied by a 80-keV isotope separator equipped with a universal ion

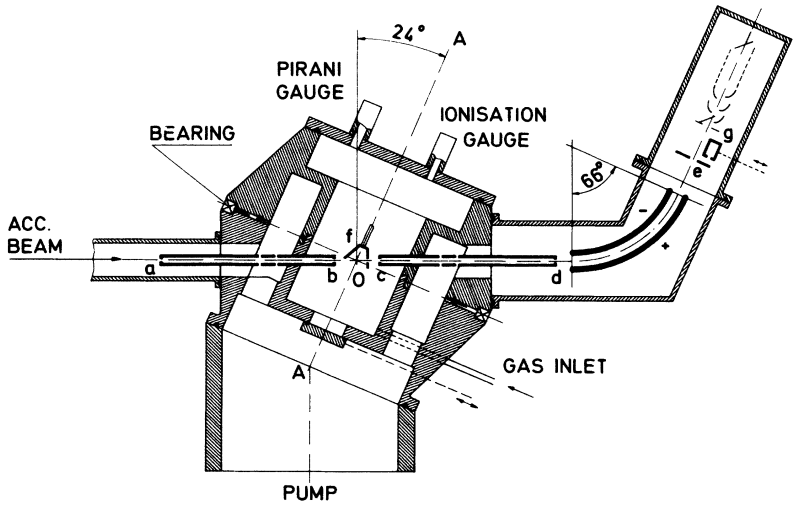

FIG. 2. Scattering chamber: a–b are the entrance collimators, f is a conically shaped Faraday cage, c and d are the exit collimators of the target, e the exit slit defining the energy resolution of the energy analyzer, and g a removable Faraday cage.

source. Ions with the desired momentum and mass are selected in a bending magnet and pass through the collimating system at the entrance of the scattering chamber (see Fig. 2).

The scattering chamber has a collimating system a-b at the entrance, a differentially pumped gas cell, a collimating system c-d at the exit, a cylindrical electrostatic analyzer, and a particle multiplier. The lower half of the scattering chamber contains the entrance collimators and is attached to the pumping system. The upper half, which includes exit collimators c-d and supports for the electrostatic analyzer, can be rotated around axis A-A without the vacuum being broken. The axis is tilted 24° from the vertical direction. The special construction of the scattering chamber allows the scattering angle to be varied from 0° to 132°, although in practice, we are not able to measure angles smaller than 4°. The entrance collimating system consists of two circular diaphragms, each of 0.5-mm diam. The distance between them is adjustable, but typically 187 mm. The path b-O-c that the particles traverse in the target gas is kept short, 23 plus 13 mm, to permit the highest possible gas pressure without violating the single-collision condition. The collimating system c-d of the scattered ions consists of two 0.5-mm-wide slits, separated by 200 mm. The slits are parallel to the z axis of the electrostatic analyzer and are always kept perpendicular to the direction of the incident beam. The electrostatic analyzer is a 120-mm-radius 66° cylindrical analyzer. The electrodes of the analyzer are 5 mm apart and are connected to a symmetric high-voltage supply. The maximum attainable voltage across the electrodes is 20 kV, corresponding to a deflection of 250-keV singly ionized particles. The analyzer has a full width resolution ΔE of $0.003E$. This is a compromise between the conflicting requirements of sufficient resolution and sufficient intensity. Ions selected by the analyzer pass an adjustable slit e, normally 0.15 mm wide, and hit the first dynode of a 17-stage particle multiplier with Cu-Be dynodes. The first dynode is kept at ground potential except when recoil particles are studied, when it has a voltage of -5 kV in order to accelerate the low-energy recoils before they hit the first dynode. The ion-electron secondary emission yield of the first dynode is high (> 10 electrons per incident particle), permitting an efficient discrimination against noise pulses, and a counting efficiency of nearly 100%. In front of the multiplier is a small removable Faraday cage g that is used to establish zero-angle settings of the chamber, and to measure the energy distribution (E_0) of the incident beam. The target cell is differentially pumped through the diaphragms of the collimators. Purified gas is admitted to the gas cell through an adjustable needle valve. The pressure of the gas in the cell is typically of the order of 3×10^{-4} Torr and measured with both a Pirani gauge and an ionization gauge to be better than 3%. The residual gas pressure is smaller than 3% of the gas pressure and does not disturb the measurements. The current of the incident beam is monitored by a special conical-shaped Faraday cage f positioned in the gas cell. The monitoring system makes it possible to continuously record the current of the incident beam.

For the special studies of the charge-state distribution of the recoils in P^+-Ar collisions, the dimensions of the collimating systems are radically changed. Diaphragms a and b are then 324 mm apart, and their diameters are 2 mm each. Slits c and d are placed 206 mm apart and are both 0.5 mm wide. The width of slit e is set to be 2 mm.

IV. EXPERIMENTAL METHOD

When the beam energy, the scattering angle, and the charge state have been set, the energy distribution of the scattered particles is measured. For fixed scattering angle and beam energy, the analyzer voltage is stepped over the voltage range necessary to cover the energy spectrum of the scattered particles. This operation is controlled by a beam-integrating system. A scaler accumulates counts from the particle multiplier until a given preset charge is collected by the beam integrator.

The number of counts is stored in a multiscaler for later readout on a punch tape. To obtain a quick survey of the measured data, a digital-analog device transforms the scaler digits to an analog voltage which is then fed to the y axis of an x-y plotter. The analyzer voltage (or, more precisely, the difference between the actual voltage and a constant voltage) is fed to the x axis of the x-y recorder such that the energy distribution of the scattered particles is plotted. The experimental setup does not allow the neutrals to be measured. As will be shown in Sec. V, this lack of information is not a serious problem in the data treatment.

The pressure of the target gas is kept sufficiently low to ensure that the scattered particles experience only one collision. To check this experimentally, the count rates of the scattered particles with charge states 1 and 4 are recorded vs pressure. Linear dependence on pressure ensures that no additional charge-changing collisions have occurred to the scattered particles. Multiple-scattering effects can be ignored since they will appear only at considerably higher gas pressures. In most cases, collisions with residual gas molecules do not distort the energy spectra. The energy spectra obtained for different scattering angles and charge states of the scattered incident particles (or the recoils) ordinarily consist of one broad peak. Although the distributions are slightly asymmetric, more pronouncedly for

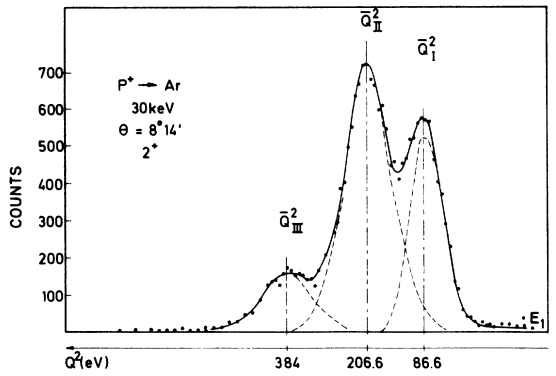

FIG. 3. Triple-peaked energy spectrum of scattered 2^+ phosphorus ions in P^+-Ar collisions at 30 keV and $\theta = 8°\ 14'$.

recoils than for scattered particles, it is a good approximation to assume a Gaussian shape. In a narrow range of r_0 values, structures with up to three peaks appear in the energy spectra. Figure 3 shows a typical triple-peaked energy spectrum of the scattered incident particles obtained in collisions between 30-keV phosphorus ions and argon atoms. Although the observed widths cause some overlap of the three distributions, it is not difficult to isolate the peaks. The recoil-energy spectra are more ambiguous to resolve, and an example of this is shown in Fig. 4. Note that the three peaks belonging to one charge state interfere with the three peaks belonging to the neighboring charge state. Spectra with two or three peaks are resolved by fitting the sum of two or three Gaussian curves to the measured energy distributions. By this computer procedure, up to nine parameters are determined: the mean energies of the peaks, $\overline{E}^m_{\rm I}$, $\overline{E}^m_{\rm II}$, and $\overline{E}^m_{\rm III}$, their widths, and their heights, where m stands for the charge state. The data are normalized with respect to target pressure and integrated beam current.

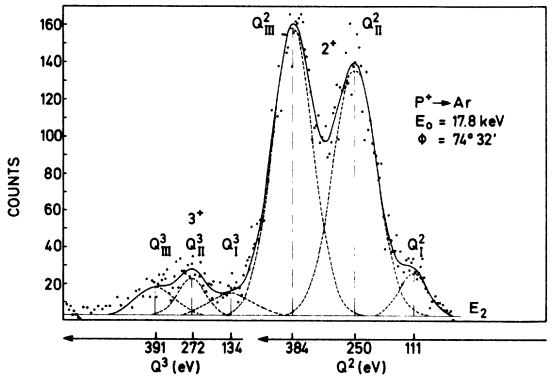

FIG. 4. Triple-peaked energy spectrum of 2^+ and 3^+ argon recoils in P^+-Ar collisions at 17.8 keV and $\phi = 74°\ 32'$.

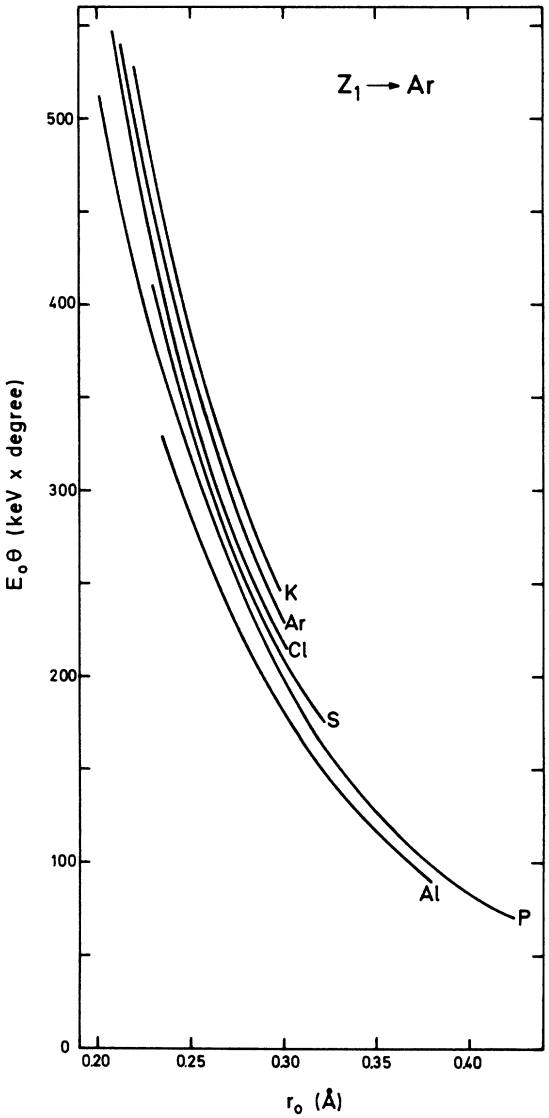

FIG. 5. Correspondence between $E_0\theta$ and the distance of closest approach in the collision r_0 for different Z_1-Ar collisions.

By means of Eq. (2) or (3), the energies of the scattered or recoil particles are transformed into inelastic energy loss Q, and hence $\overline{E}^m_j$ is converted into $\overline{Q}^m_j$. The "area" of peak j, representing all scattered particles with charge state m and energy loss Q^m_j, is denoted by N^m_j.

From $\overline{Q}^m_j$ and N^m_j data taken at various scattering angles and incident energies, we derive (a) the probability that the scattered particles have been Q_j-excited and are in charge state m

$$P^m_j = N^m_j \Big/ \sum_{m,j} N^m_j \ ;$$

(b) the mean inelastic energy loss $\overline{Q}_j$ averaged over

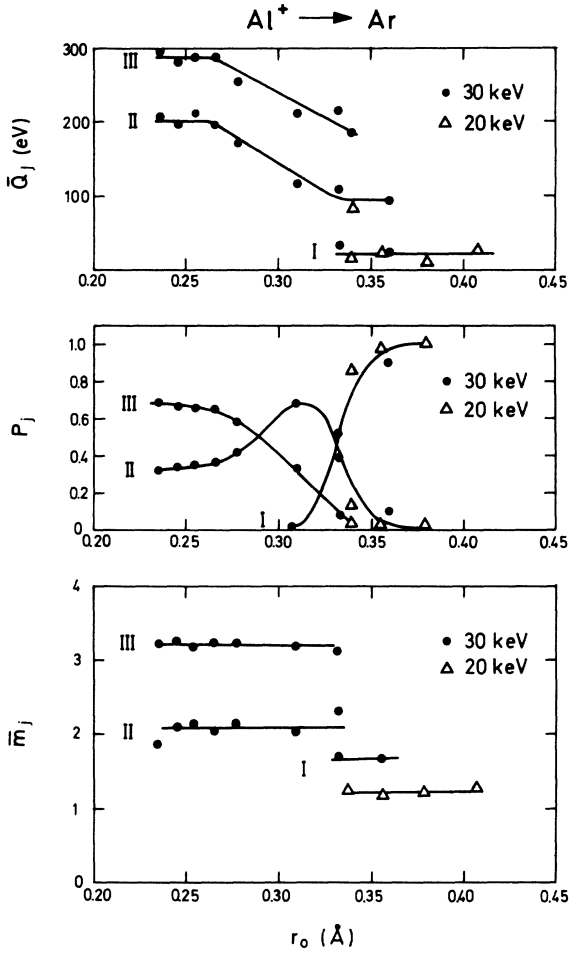

FIG. 6. Al^+-Ar: mean inelastic energy loss $\bar{Q}_j$, excitation probability P_j, and mean charge state $\bar{m}_j$ of the scattered aluminum particles at 20- and 30-keV incident energy, represented by △ and •, respectively.

the charge-state distribution is

$$\bar{Q}_j = \sum_m P_j^m \bar{Q}_j^m \Big/ \sum_m P_j^m ;$$

(c) the charge-state distributions of Q_j-excited scattered particles

$$P_j(m) = P_j^m \Big/ \sum_m P_j^m ;$$

(d) the probability of a Q_j excitation

$$P_j = \sum_m P_j^m ;$$

and (e) the mean charge state of the scattered Q_j-excited particles

$$\bar{m}_j = \sum_m P_j^m m \Big/ \sum_m P_j^m .$$

In the case of recoil particles, m is replaced by n, the charge state of the recoils.

The presentation of the data will include plots of $\bar{Q}_j$, P_j, $\bar{m}_j$, and $P_j(m)$ against the distance of closest approach r_0. The P_j^m probabilities may then be evaluated from the formula $P_j^m = P_j \times P_j(m)$. The measured $\bar{Q}_j^m$ values increase slightly with the charge state m, although the shift is small compared with their mean value $\bar{Q}_j$. For the sake of brevity, these data are not listed in the paper.

For small scattering angles θ, it is well known

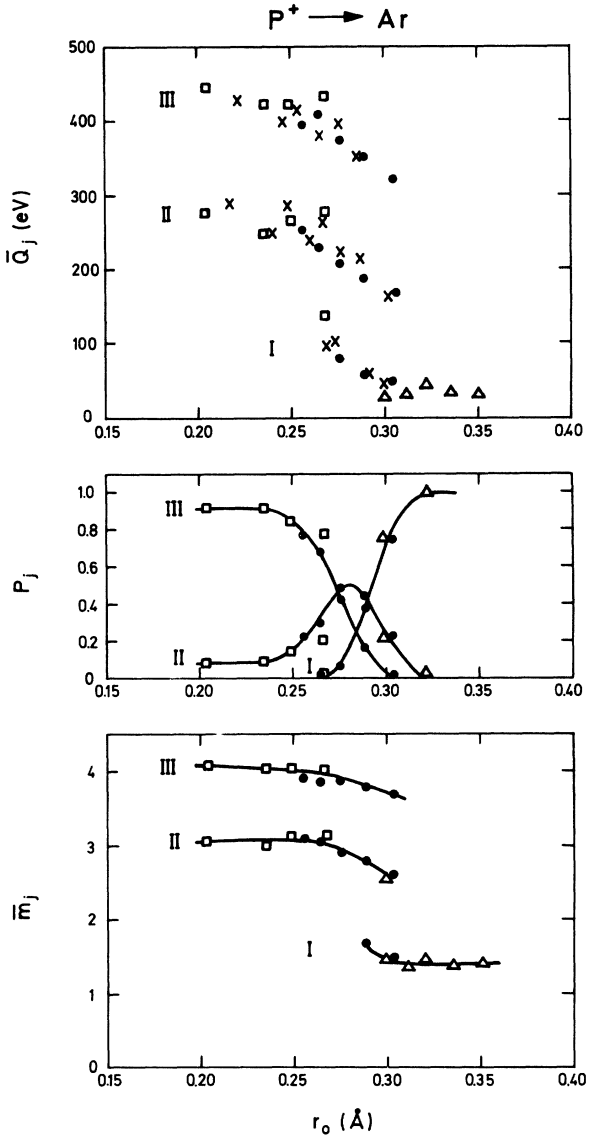

FIG. 7. P^+-Ar: mean inelastic energy loss $\bar{Q}_j$, excitation probability P_j, and mean charge state $\bar{m}_j$ of the scattered phosphorus particles at 20-, 30-, and 50-keV incident energy, represented by △, •, and □, respectively. Also shown are $\bar{Q}_j$ values obtained from energy analysis of recoil particles at 17.8- and 19.3-keV (×) incident energy.

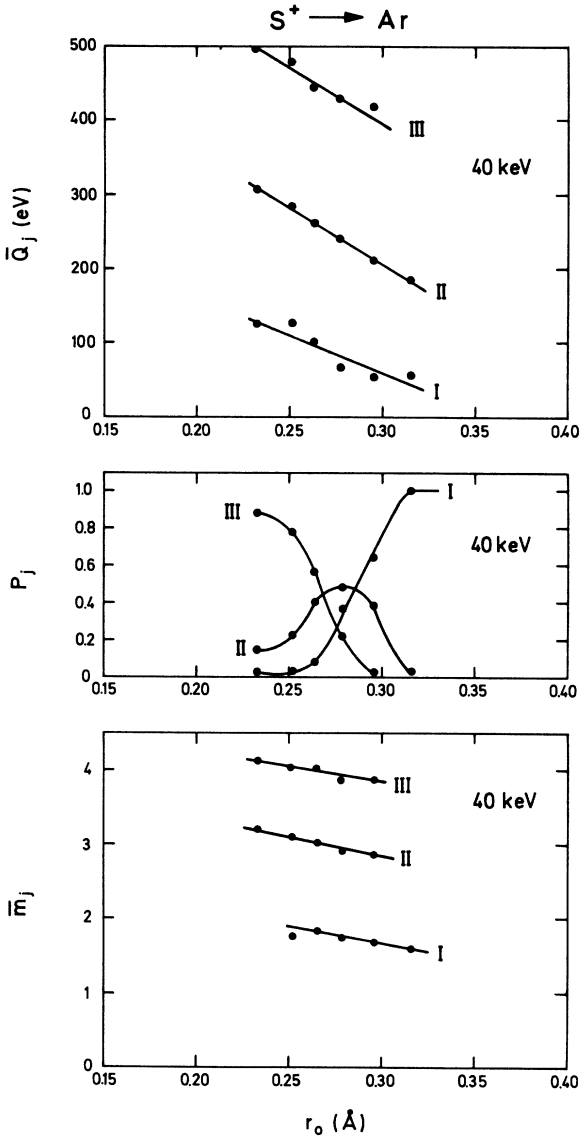

FIG. 8. S^+-Ar: mean inelastic energy loss $\bar{Q}_j$, citation probability P_j, and corresponding mean charge state $\bar{m}_j$ of the scattered sulphur particles at 40-keV incident energy.

that r_0 depends primarily on the product $E_0\theta$. However, in order to facilitate a comparison with earlier data, the r_0 calculations have been based on an exponentially screened Coulomb potential.[25] Recent experiments by Loftager and Claussen[26] on the total differential-scattering cross section, however, have shown that cross sections based on the exponentially screened Coulomb potential may be as much as 30% off the measured values. Therefore, the calculated r_0 is only a rough estimate of the real distance of closest approach. Figure 5 shows r_0 as a function of $E_0\theta$ for various Z_1-Ar combinations.

V. WIDTH OF SPECTRAL LINES

The observed linewidths in the Q spectra are the result of a natural linewidth ($\delta Q_{\rm nat}$), instrumental resolution ($\delta Q_{\rm instr}$), and thermal target motion (δQ_T). Assuming that the three contributions are uncorrelated, one obtains

$$\delta Q^2_{\rm obs} = \delta Q^2_{\rm nat} + \delta Q^2_{\rm instr} + \delta Q^2_T \ .$$

An apparent single Q line with a Gaussian shape may actually be a weighted sum of several closely spaced lines, all resulting in the same charge state for the scattered particles. This means that $\delta Q_{\rm nat}$ is the width of an unresolved distribution consisting of

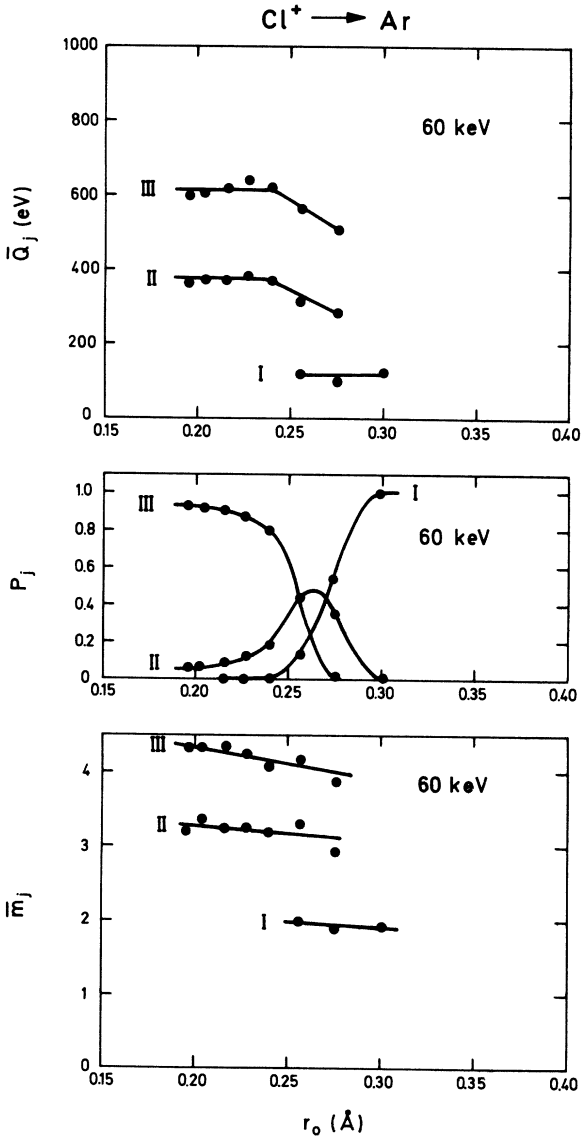

FIG. 9. Cl^+-Ar: mean inelastic energy loss $\bar{Q}_j$, excitation probability P_j, and mean charge state $\bar{m}_j$ of the scattered chlorine particles at 60-keV incident energy.

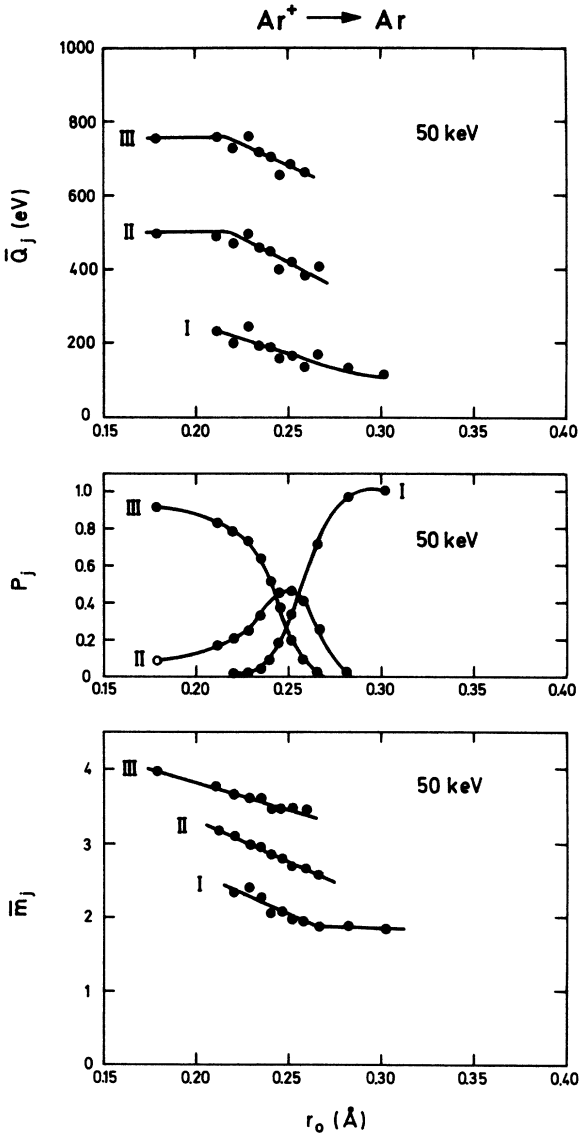

FIG. 10. Ar^+-Ar: mean inelastic energy loss $\bar{Q}_j$, excitation probability P_j, and mean charge state $\bar{m}_j$ of the scattered argon particles at 50-keV incident energy.

several closely spaced lines. The instrumental resolution $\delta Q_{\text{instr}} \sim 0.1$–$0.2\%$ (half-width at $1/e$ height) accounts almost exclusively for the observed widths; hence, it is not possible to derive reliable natural widths from the data.

VI. ERROR ANALYSIS

The main errors in the data come from fluctuations and long-term drifts of beam energy, analyzer voltage, etc. The fluctuations are small, and the long-term drifts of beam energy and analyzer voltage are frequently checked by measuring the energy distribution of the incident beam. The rotation angle of the scattering chamber is determined to be better than 3′. The computational decomposition of the peaked structure adds some uncertainty, particularly in cases where a high peak dominates a small peak, and appreciable errors in the determination of the N_j^m and $\bar{Q}_j^m$ data may result. The averaged quantities $\bar{Q}_j$, P_j, and $\bar{m}_j$, however, are more accurate. The lack of information on the neutrals may cause some systematic errors in the charge-state distributions. These errors, causing higher values of the mean charge state, are significant only in cases where the mean charge is less than 1.5 charge unit, i.e., for $\bar{m}_I$ at large r_0. Since the

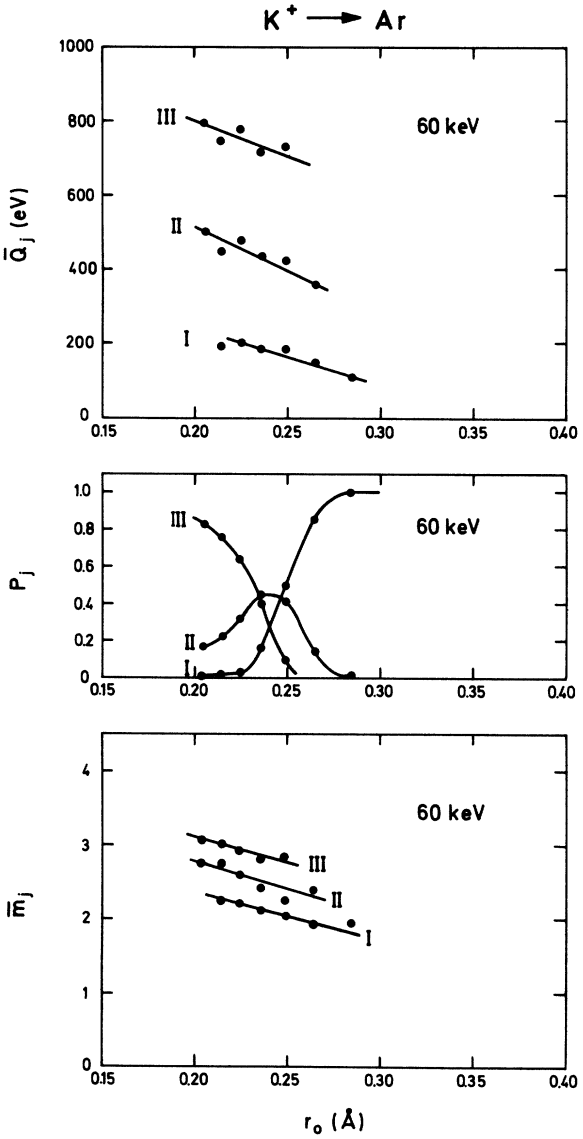

FIG. 11. K^+-Ar: mean elastic energy loss $\bar{Q}_j$, the excitation probability P_j, and the mean charge state $\bar{m}_j$ of the scattered potassium particles at 60-keV incident energy.

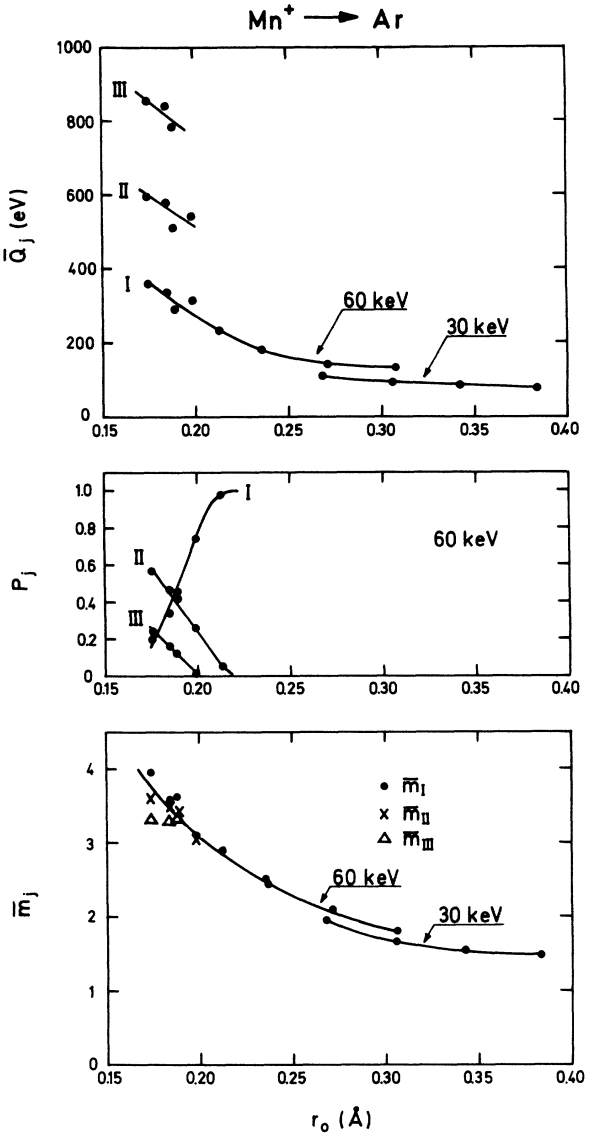

FIG. 12. Mn^+-Ar: mean inelastic energy loss $\bar{Q}_j$, excitation probability P_j, and mean charge state $\bar{m}_j$ of the scattered manganese particles at 30- and 60-keV incident energy.

values of $\bar{m}_{II}$ and $\bar{m}_{III}$ are, however, both larger than 1.5, they are reliable.

VII. RESULTS AND DISCUSSION

The data on the three inelastic energy losses $\bar{Q}_I$, $\bar{Q}_{II}$, and $\bar{Q}_{III}$, their excitation probabilities P_I, P_{II}, and P_{III}, and the corresponding mean charge states of the scattered incident particles $\bar{m}_I$, $\bar{m}_{II}$, and $\bar{m}_{III}$ are shown in Figs. 6–12. From the data, several observations can be made. First, it is evident that in all collisional cases, a narrow range of distances of closest approach r_0 exists, where the energy-loss spectrum is triple-peaked. At high r_0 outside the triple-peaked region, P_I is unity, i.e., that only Q_I excitations prevail. At low r_0 outside the triple-peaked region, P_I is zero and P_{III} close to unity, i.e., the excitation predominantly is of type Q_{III}. In the case of Al^+-Ar, however, a substantial Q_{II} excitation ($P_{II} \simeq 0.4$) is also present at low r_0. Although the three Q_j values decrease with increasing r_0, their differences $\bar{Q}_{II} - \bar{Q}_I$ and $\bar{Q}_{III} - \bar{Q}_{II}$ remain independent of r_0. $\bar{Q}_{III} - \bar{Q}_{II}$ is approximately 20% larger than $\bar{Q}_{II} - \bar{Q}_I$ with Ar^+-Ar as the only exception where the differences are equal. In all cases, except Al^+-Ar, it is seen that P_{II} reaches a maximum value of 0.5 in the center of the triple-peaked Q region. For Al^+-Ar, the corresponding figure is 0.7.

The mean charge states $\bar{m}_I$, $\bar{m}_{II}$, and $\bar{m}_{III}$, which are almost independent of r_0 for the lighter projectile, i.e., Al^+ and P^+, seem to become r_0 dependent with increasing atomic number of the projectile.

The differences $\bar{m}_{II} - \bar{m}_I$ and $\bar{m}_{III} - \bar{m}_{II}$ are both approximately unity for the lighter projectiles such as Al^+, P^+, and S^+. For the heavier projectiles, the differences get smaller and approach zero for the Mn^+-Ar case. The detailed charge-state distributions of the scattered incident particles $P_j(m)$ are shown in Figs. 13–18.

In the study of ejected electrons, most effort is concentrated on the investigations of the Auger electrons, resulting from the decay of inner-shell vacancies produced in the colliding atoms. In all cases studied, a broad-peaked electron-energy distribution is seen. Possible fine structures in the spectra are not seen, due partly to a poor (4–5%) energy resolution of the electron spectrometer.

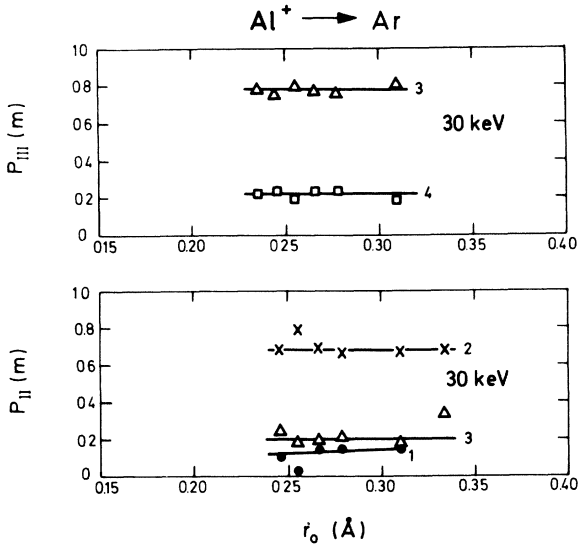

FIG. 13. Al^+-Ar: charge-state distribution $P_j(m)$ of the Q_j-excited scattered aluminum particles at 30-keV incident energy.

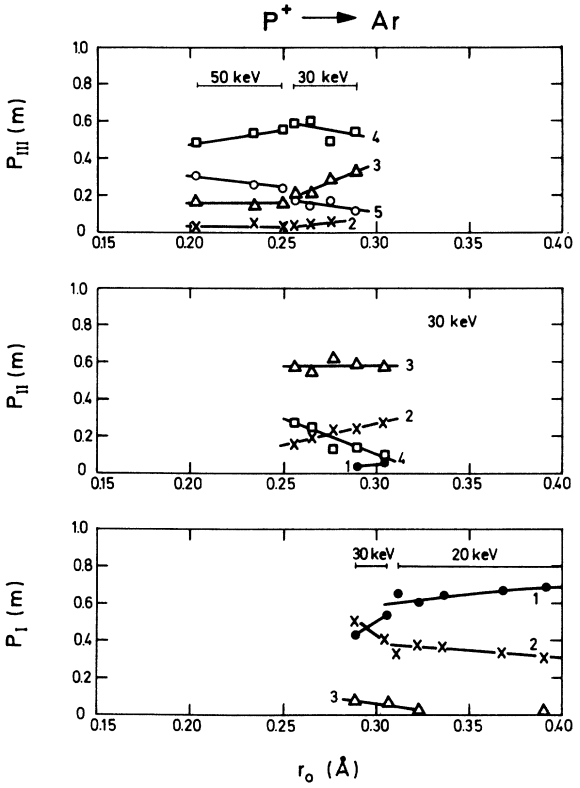

FIG. 14. P⁺-Ar: charge-state distribution $P_j(m)$ of the Q_j-excited scattered phosphorus particles at 20-, 30-, and 50-keV incident energy.

It is recognized that the Q data on heteronuclear collisions have much in common with earlier data of Ar^+-Ar,[2] where it was found that the triple-peaked Q structure was a result of the promotion of one or two $L_{2,3}$ electrons during the collision.[4] We have therefore adopted a promotion model, where a Q_{II} excitation involves the promotion of one $L_{2,3}$ electron, and a Q_{III} excitation the promotion of two $L_{2,3}$ electrons. For the Ar^+-Ar collision it is natural to think that the promotion can take place with equal probability in either atom. For the heteronuclear collisions, where the $L_{2,3}$ binding energies are different for the two colliding particles, the situation is more complicated. To decide whether the $L_{2,3}$ vacancies are produced in either or in both colliding particles, we have compared the Q_j differences $\overline{Q}_{II}-\overline{Q}_I$, $\overline{Q}_{III}-\overline{Q}_{II}$, and $\overline{Q}_{III}-\overline{Q}_I$ with the binding energies of one and two $L_{2,3}$ electrons in both the projectile and the target atom (see Table I). The binding energy of two $L_{2,3}$ electrons has been estimated from transition energies of $KL_{2,3}L_{2,3}$ Auger processes and K binding energies. Also shown in Table I are the experimental data on the mean energy of Auger electrons ejected in the collisions. Except for the Ar^+-Ar case, where good agreement with earlier electron data[17] is established, we are not able to compare our data with earlier measurements.

In the following discussion, it is convenient to divide the collisions into three groups.

1. *Collisions with* $Z_1 < Z_2 - 1$

It is seen from Table I that $\overline{Q}_{II}-\overline{Q}_I$ compares well with the binding energy of an $L_{2,3}$ electron in the projectile atom. $\overline{Q}_{III}-\overline{Q}_{II}$ is considerably smaller than the binding energy of an $L_{2,3}$ electron in the target atom, but compares well with the energy necessary to remove a second $L_{2,3}$ electron in the projectile. This energy is estimated to be some 20–40% higher than the binding energy of the first $L_{2,3}$ electron. The data therefore suggest that Q_I correspond to M-shell excitations in both collision partners, Q_{II} to M-shell excitations plus the pro-

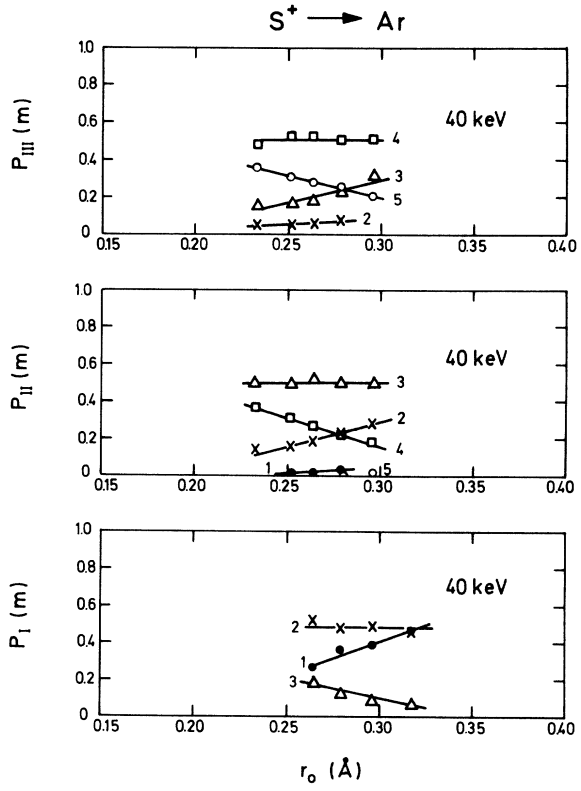

FIG. 15. S⁺-Ar: charge-state distribution $P_j(m)$ of the Q_j-excited scattered sulphur particles at 40-keV incident energy.

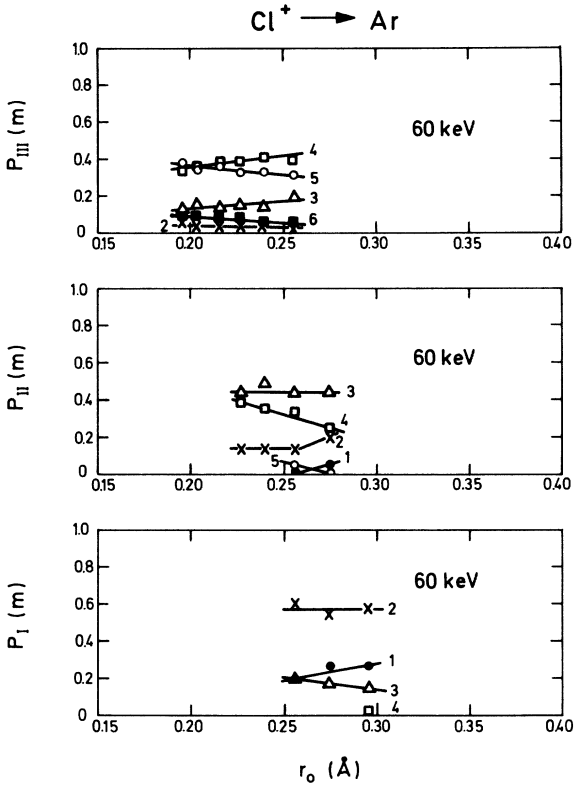

FIG. 16. Cl^+-Ar: charge-state distribution $P_j(m)$ of the Q_j-excited scattered chlorine particles at 60-keV incident energy.

motion of one $L_{2,3}$ electron in the projectile (the lower-Z partner), and Q_{III} to M-shell excitation plus the promotion of two $L_{2,3}$ electrons in the projectile. The $L_{2,3}$ vacancies decay preferentially via Auger transitions, such that the decay of one and two vacancies raises the charge state of the particle by one and two charge units, respectively. The promotion model is further supported by the charge-state data. If we consider the S^+-Ar case (see Fig. 15), it is noted that the charge-state distributions $P_I(m)$, $P_{II}(m)$, and $P_{III}(m)$ for all m obey the rule

$$P_I(m) = P_{II}(m+1) = P_{III}(m+2) \quad (4)$$

fairly well, implying that $\overline{m}_{III} = \overline{m}_{II} + 1 = \overline{m}_I + 2$. The S^+-Ar data agree surprisingly well with the last equality in Eq. (4), and the first equality is at least qualitatively fulfilled. Because Q_{II} and Q_{III} excitations involve one and two $L_{2,3}MM$ Auger transitions, respectively, we may conclude that after separation of the colliding particles, but before the Auger decay, the charge-state distribution of the projectile particles is independent of the excitation Q_j and given by $P_I(m)$. This means that the $L_{2,3}$ electrons are promoted without changing the charge state. For Al^+-Ar and P^+-Ar collisions, the last equality in Eq. (4) is qualitatively fulfilled, i.e., $P_{II}(m+1) = P_{III}(m+2)$. The charge-state data of argon recoils in P^+-Ar collisions (Fig. 19), showing that $\overline{n}_j$ is independent of Q_j, indicate that the mean charge state of the collision partner with the higher Z is independent of the excitation Q_j, i.e., $\overline{n}_I \simeq \overline{n}_{II} \simeq \overline{n}_{III}$. This is in accordance with the hypothesis that no inner-shell vacancies are produced in the higher-Z collision partner. Furthermore, it is seen that $\overline{n}_j$ is strongly dependent on r_0, i.e., that it decreases with increasing r_0.

Doppler-shift analysis of the electron spectra shows unambiguously that the fast Auger electrons are emitted from the projectiles only. The mean energy of these electrons agrees well with the expected kinetic energy of an $L_{2,3}MM$ Auger electron from the projectile (the lower-Z partner).

2. *Collisions with* $Z_1 = Z_2 - 1$, $Z_1 = Z_2$, *and* $Z_1 = Z_2 + 1$

In the three intermediate cases, the atomic numbers of the colliding particles differ by no more than one. Let us first see what can be concluded from the Q data.

Cl^+-Ar. From Table I it is seen that $\overline{Q}_{II} - \overline{Q}_I$ is in good agreement with the binding energy of an $L_{2,3}$

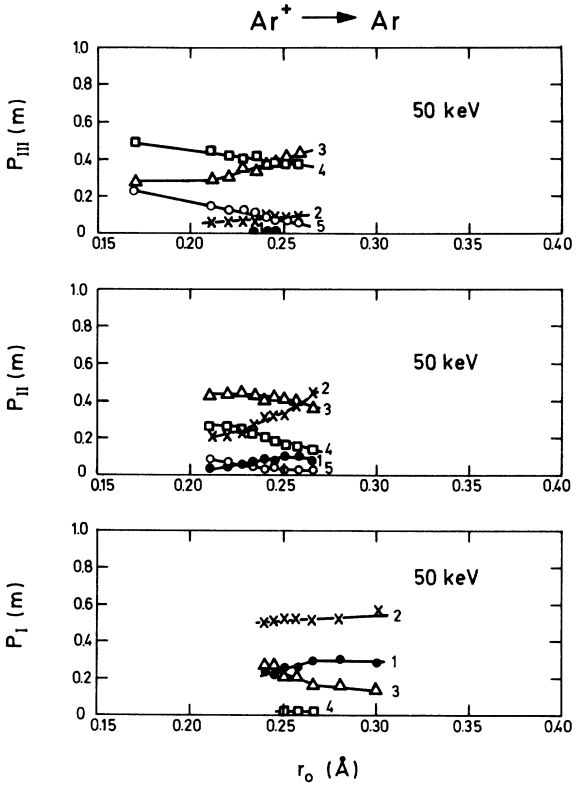

FIG. 17. Ar^+-Ar: charge-state distribution $P_j(m)$ of the Q_j-excited scattered argon particles at 50-keV incident energy.

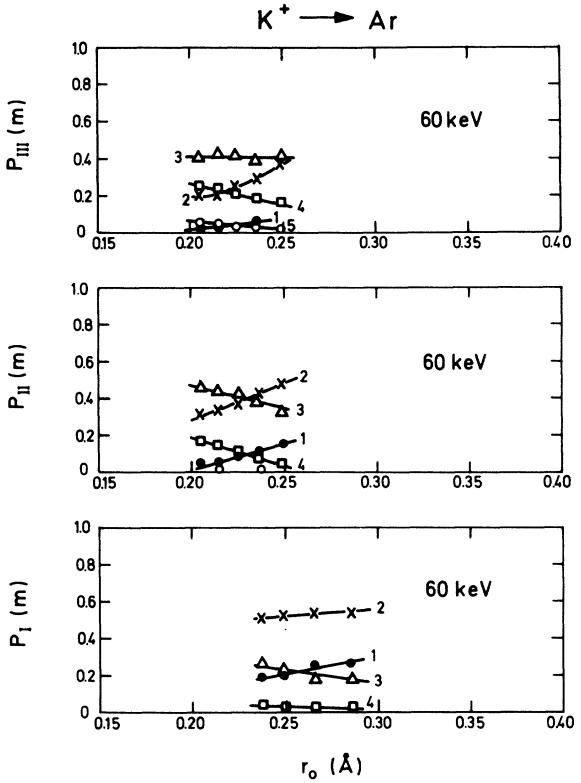

FIG. 18. K^+-Ar: charge-state distribution $P_j(m)$ of the Q_j-excited scattered potassium particles at 60-keV incident energy.

electron in chlorine. As the binding energy of an $L_{2,3}$ electron in argon is only 20% larger than that in chlorine, we cannot at this stage rule out the possibility that Q_{II} excitations in some cases may result in the promotion of one $L_{2,3}$ electron in argon (the higher-Z partner). It is further seen that $\bar{Q}_{III} - \bar{Q}_{II}$ being 25% higher than $\bar{Q}_{II} - \bar{Q}_{I}$ compares well with both the binding energy of an $L_{2,3}$ electron in argon and the binding energy of the second $L_{2,3}$ electron in chlorine (estimated to be approximately 240 eV). The mean charge state $\bar{m}_j$ shows characteristics similar to what is observed for the $Z_1 < Z_2 - 1$ case, namely, that $\bar{m}_{III} - \bar{m}_{II}$ and $\bar{m}_{II} - \bar{m}_{I}$ both approximate unity.

The electron-spectra studies show that the majority of the Auger electrons are ejected from scattered chlorine, whereas a minor fraction of the Auger electrons are ejected from argon recoils. Hence, we may conclude that most Q_{II} excitations involve a promotion of one $L_{2,3}$ electron in chlorine, and most Q_{III} excitations involve the promotion of two $L_{2,3}$ electrons in chlorine.

The Ar^+-Ar collisions have already been discussed.[1,2] Here we want, however, to present some of the new observations. It is seen that $\bar{Q}_{II} - \bar{Q}_{I} = \bar{Q}_{III} - \bar{Q}_{II} = 254 \pm 20$ eV, which agrees well with the

TABLE I. Presentation of the $\bar{Q}_j$ and $\bar{m}_j$ differences and the Auger electron energies for the various collision cases studied. r_0 corresponds to the center of the triple-peaked Q region (P_{II} at maximum). $B_{L_{2,3}}(Z_1)$ and $B_{L_{2,3}L_{2,3}}(Z_1)$ are the binding energies of one and two $L_{2,3}$ electrons in the projectile atom. The energy interval stated for the $B_{L_{2,3}L_{2,3}}(Z_1)$ shows the multiplet splitting. $E_{el}(Z_1)$ and $E_{el}(Z_2)$ are the mean kinetic energies of LMM Auger electrons ejected from the scattered incident particles and from the recoil particles, respectively. A "no" in the two last columns means that no Auger electrons are found. The Q differences listed for the P^+-Ar case are taken from the scattered incident-particle data.

Z_I	E_0 (keV)	r_0 (Å)	$\bar{Q}_{II} - \bar{Q}_{I}$ (eV)	$\bar{Q}_{III} - \bar{Q}_{II}$ (eV)	$\bar{Q}_{III} - \bar{Q}_{I}$ (eV)	$\bar{m}_{II} - \bar{m}_{I}$	$\bar{m}_{III} - \bar{m}_{II}$	$\bar{n}_{II} - \bar{n}_{I}$	$\bar{n}_{III} - \bar{n}_{II}$	$B_{L_{2,3}}(Z_1)$ (eV)	$B_{L_{2,3}L_{2,3}}(Z_1)$ (eV)	$E_{el}(Z_1)$ (eV)	$E_{el}(Z_2)$ (eV)
13	20/30	0.31	70 ± 10	90 ± 10	160 ± 10		1.1	...	...	78	168–181	63	no
15	20/30/50	0.285	127 ± 10	168 ± 10	295 ± 10	1.1	1.0	0	0	137	297–314	98	no
16	40	0.275	160 ± 10	200 ± 10	360 ± 10	1.2	1.0	...	...	167	357–376	118	no
17	60	0.263	190 ± 15	238 ± 15	428 ± 15	1.2	1.0	...	...	204	432–453	137	171
18	50	0.247	254 ± 20	254 ± 20	508 ± 20	0.7	0.65	...	...	250	524–547	171	171
19	60	0.238	246 ± 20	294 ± 20	540 ± 20	0.35	0.35	...	...	300	624–649	200	169
25	60	~0.16	233 ± 30	267 ± 30	500 ± 30	0	0	...	...	650	1328–1370	no	157

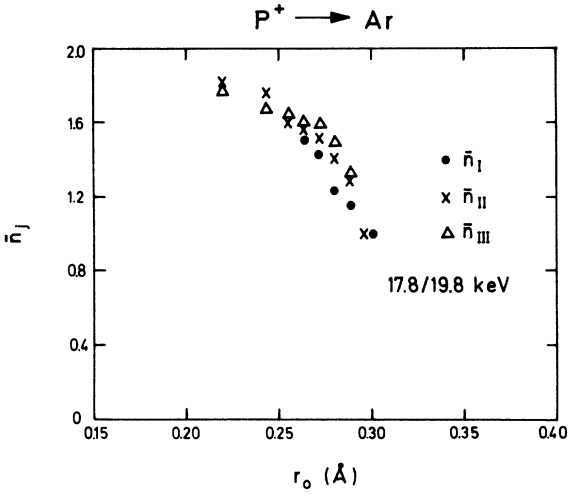

FIG. 19. P^+-Ar: mean charge states $\bar{n}_j$ of the Q_j-excited argon recoils at 17.8- and 19.8-keV incident energy.

binding energy of an $L_{2,3}$ electron in argon (250 eV). The mean charge states $\bar{m}_I$, $\bar{m}_{II}$, and $\bar{m}_{III}$ decrease with increasing r_0. Their differences $\bar{m}_{II} - \bar{m}_I$ and $\bar{m}_{III} - \bar{m}_{II}$ are 0.7 and 0.65, respectively. Assuming that the recoils have the same charge-state distribution as the incident scattered particles, i.e., $\bar{n}_{III} \simeq \bar{m}_{III}$, $\bar{n}_{II} \simeq \bar{m}_{II}$, etc., it is found that the total mean charge state $\bar{m}_{III} + \bar{n}_{III}$ of the two colliding particles in a Q_{III} excitation is 1.3 higher than the corresponding figure $\bar{m}_{II} + \bar{n}_{II}$ for a Q_{II} excitation. In a Q_{II} excitation, the total mean charge state is still 1.4 higher than that obtained in a Q_I excitation. These results differ from what is observed for the cases $Z_1 \leq Z_2 - 1$, where the change of the total mean charge state from a Q_I to a Q_{II} excitation or from a Q_{II} to a Q_{III} excitation is unity. However, in the explanation of this "anomaly", several factors may play a role: In some cases, an $L_{2,3}$ electron is promoted into the continuum, thereby raising the total charge state by unity. In a few cases, the Auger transitions may result in the ejection of more than one electron.[18]

The K^+-Ar collision data show that $\bar{Q}_{II} - \bar{Q}_I$ equals the $L_{2,3}$ binding energy in the argon recoils. Hence, we can conclude that a Q_{II} excitation most probably results in a promotion of one $L_{2,3}$ electron in argon. We can, however, not completely rule out the alternative possibility that the $L_{2,3}$ vacancy is produced in potassium, the other collisional partner. $\bar{Q}_{III} - \bar{Q}_{II}$ being 20% higher than $\bar{Q}_{II} - \bar{Q}_I$ compares well with both the binding energy of an $L_{2,3}$ electron in potassium (300 eV) and the binding energy of a second $L_{2,3}$ electron in argon (estimated to be 300 eV).

The mean charge state $\bar{m}_j$ of the scattered potassium particles shows that $\bar{m}_{III} - \bar{m}_{II} \simeq \bar{m}_{II} - \bar{m}_I \simeq 0.35$-0.4, or midway between the corresponding figures 0.7 and 0 for the Ar^+-Ar and Mn^+-Ar cases. This indicates roughly that in Q_{II} and Q_{III} excitations, one quarter of the $L_{2,3}$ vacancies are produced in the potassium particles and three quarters in the argon recoils. An admixture of $L_{2,3}$ excitations in potassium will cause a high-energy tail in the Q_{II} distribution. Because of an overlap of the Q_{II} and Q_{III} distributions, we have, however, not been able to resolve any significant asymmetry in the measured Q_{II} distribution.

3. *Collisions with* $Z_1 > Z_2 + 1$

The only case studied is Mn^+-Ar collisions ($Z_1 = 25$). From Table I is noted that $\bar{Q}_{II} - \bar{Q}_I$ agrees well with the binding energy of an $L_{2,3}$ electron in argon, whereas the corresponding binding energy in manganese is more than twice as high as $\bar{Q}_{II} - \bar{Q}_I$. We may therefore conclude that Q_{II} involves a promotion of one $L_{2,3}$ electron in argon, the colliding particle with the lower Z. By similar reasoning it is seen that $\bar{Q}_{III}$ involves the promotion of two $L_{2,3}$ electrons in argon. The charge-state analysis of the scattered manganese ions, showing that the mean charge state $\bar{m}_j$ is independent of the excitation Q_j, confirms that neither Q_{II} nor Q_{III} excitations produce $L_{2,3}$ vacancies in manganese. It is noted that $\bar{m}_j$ depends strongly on r_0. Electron-spectra data, including Doppler-shift analysis, support these findings.

The production of two $L_{2,3}$ vacancies in one atom raises the question whether they are produced by two independent one-electron promotions. In Ar^+-Ar collisions, where a Q_{III} excitation produces one vacancy in both argon atoms, Kessel and Everhart[2] applied with great success a one-electron promotion probability $\alpha(r_0)$ to account for the excitation probabilities P_I, P_{II}, and P_{III}. In terms of α, $P_I = (1-\alpha)^2$, $P_{II} = 2\alpha(1-\alpha)$, and $P_{III} = \alpha^2$, where α runs from 0 to 1. It is immediately recognized that P_{II} reaches a maximum of 0.5 for $\alpha = \frac{1}{2}$, and that $P_I = P_{III} = 0.25$ for the same value of α. Since all the P_j data on heteronuclear collisions but Al^+-Ar comply with these prescriptions, we have adopted the Kessel-Everhart procedure to reduce the excitation probabilities P_I, P_{II}, and P_{III} to a one-electron promotion probability $\alpha(r_0)$. The analysis gives unambiguous $\alpha(r_0)$ values and thereby confirms that double vacancies are produced by two independent one-electron promotions. The $\alpha(r_0)$ curves are shown in Fig. 20.

The r_0 range for which the triple-peaked Q region occurs corresponds to an interpenetration of the $L_{2,3}$ subshells of the colliding particles. For the different collisions Z_1-Ar (excluding Al^+-Ar), Fig. 21 shows a comparison between the r_0 value at which $\alpha(r_0) = \frac{1}{2}$ and the sum of the radii of $2p$ electronic orbits in the colliding particles. The radius of the

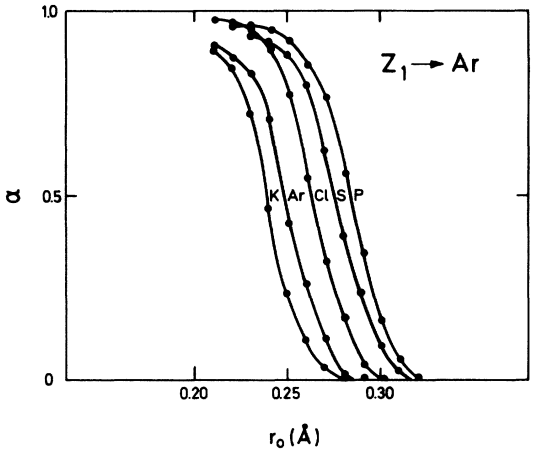

FIG. 20. Single $L_{2,3}$ electron promotion probability $\alpha(r_0)$ as a function of r_0.

$2p$ electronic orbit resents the distance from the nucleus at which the radial-charge density is at maximum. It is noted that the triple-peaked Q region corresponds to a considerable interpenetration of the $L_{2,3}$ subshells.

The data on the excitation probabilities P_j make it straightforward to calculate Auger-emission cross sections. The number of emitted Auger electrons is $2P_{III} + P_{II} = 2\alpha(r_0)$, so the differential cross section is

$$d\sigma = 4\pi\alpha(r_0)pdp \ ,$$

where p is the impact parameter which, for a given interaction potential, can be derived from r_0.

The similarity between excitation probabilities P_j of homonuclear and heteronuclear collisions suggests that inner-shell vacancies in heteronuclear collisions are produced by crossings of MO's. Unfortunately, to the knowledge of the authors, no published calculations exist of energy curves of single-electron MO's for heteronuclear systems including argon. The Landau-Zener model, where the promotion probability at the most is 50%, is not consistent with the measured data on the production efficiency of $L_{2,3}$ vacancies. The almost 100% efficiency at small r_0 may be a result of many crossings. Within the limited velocity range used in the measurements, we have not been able to detect any significant velocity effect in the excitation probabilities. However, a comparison of $\alpha(r_0)$ curves for Ar^+-Ar obtained by Kessel and Everhart[2] at 25 keV and by us at 50 keV indicates a small but definite shift, such that the r_0 value at which $\alpha(r_0) = \frac{1}{2}$ moves toward higher r_0 for increasing velocities. The maximum value of $\alpha(r_0)$ around 0.95 seems, however, not to be affected by a velocity change. Three results from the previous discussion are important to note: (i) In all the measured collisions, the promoted electrons are $2p$ electrons; (ii) at most, two $2p$ electrons are promoted per collision, suggesting that these electrons are $2p\sigma$ electrons; and (iii) the promoted $2p$ electron comes from the lower-Z collision partner.

VIII. CONCLUSIONS

For all the collisions, a narrow range of r_0 values exists where the Q structure is triple-peaked.

$\bar{Q}_{II} - \bar{Q}_I$ and $\bar{Q}_{III} - \bar{Q}_{II}$ are both constant over the triple-peaked Q region. $\bar{Q}_{III} - \bar{Q}_{II}$ is some 20% larger than $\bar{Q}_{II} - \bar{Q}_I$.

$\bar{Q}_{II} - \bar{Q}_I$ is approximately equal to the binding energy of one $L_{2,3}$ electron, and $\bar{Q}_{III} - \bar{Q}_I$ is approximately equal to the total binding energy of two $L_{2,3}$ electrons in the collisional partner with the lower atomic number.

In the cases Cl^+ and K^+ on Ar, $L_{2,3}$ vacancies are produced in both colliding particles. The majority of $L_{2,3}$ vacancies is, however, produced in the partner with the lower Z. For Ar^+-Ar collisions, $L_{2,3}$ vacancies are produced with equal probabilities in both colliding particles.

With due reference to the statements above we find that Q_I excitation corresponds to M-shell excitations in both colliding particles. Q_{II} excitation corresponds to Q_I excitation plus the production of one $L_{2,3}$ vacancy in the collision partner with the lower atomic number. Q_{III} excitation corresponds to Q_I excitation plus the production of two $L_{2,3}$ vacancies in the collision partner with the lower atomic number.

Studies of electron spectra have confirmed these findings, and the fast-electron group has been shown to comply with $L_{2,3}MM$ Auger electrons.

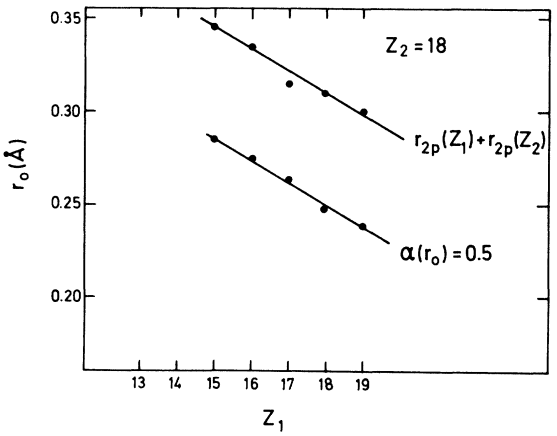

FIG. 21. Comparison of the r_0 value at which $\alpha(r_0) = \frac{1}{2}$, corresponding to the center of the triple-peaked Q region, with the sum of the radii of $2p$ electronic orbits in the projectile atom and the target atom.

Charge-state studies have shown that in the lower-Z partner, Q_{III} excitations produce a mean charge state which is one higher than the mean charge state produced by a Q_{II} excitation, and which, again, is one higher than the mean charge state produced in a Q_I excitation. For the higher-Z partner, the mean charge state is almost independent of the excitation Q_j. The charge-state analysis further shows that the mean charge state of the lower-Z partner is almost independent of r_0, whereas for the higher-Z partner, the mean charge state shows a strong r_0 dependence. These statements do not hold for $Z_1 = Z_2 - 1$, Z_2, or $Z_2 + 1$.

We want to emphasize here that the conclusions we have drawn are based on studies of collisions where argon is one of the colliding particles and the other particle is an atom with a filled L shell and an incompletely filled M shell.

ACKNOWLEDGMENTS

The authors acknowledge enlightening discussions with numerous colleagues, in particular, P. Dahl and D. C. Lorents. The patient and efficient assistance of members of the accelerator group is gratefully appreciated.

APPENDIX: EFFECT OF THERMAL TARGET MOTION ON Q SPECTRA

Figure 22 shows the momentum quadrangle in a collision. Here, $\vec{P}_0$, $\vec{P}_1$, and $\vec{P}_2$ are the linear momenta of the incident, the scattered, and the recoil particles, respectively. $\vec{P}_T$ is the momentum of the target particle due to its thermal motion. Its projections are $P_{x,T} = \alpha_x P_0$, and $P_{y,T} = \alpha_y P_0$. The third component $P_{z,T}$ may be ignored because, to a first-order approximation, it affects only the intensity of particles being scattered into the analyzer.

Conservation of momentum yields the two equations

$$(1 + \alpha_x)(\gamma E_0)^{1/2} = (\gamma E_1)^{1/2}\cos\theta + E_2^{1/2}\cos\phi \ , \quad \text{(A1)}$$

$$(\gamma E_1)^{1/2}\sin\theta = E_2^{1/2}\sin\phi + \alpha_y(\gamma E_0)^{1/2} \ . \quad \text{(A2)}$$

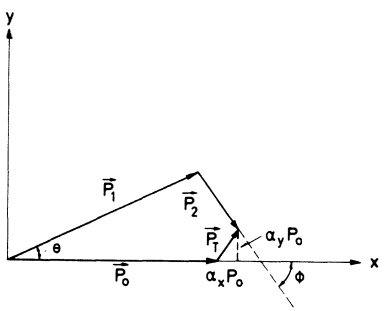

FIG. 22. Effect of the thermal target momentum on the momenta of the scattered particles.

1. *Scattered-Particle Method*

Eliminating ϕ and discarding second-order terms in α_x and α_y gives

$$E_2 = -2\gamma(E_0E_1)^{1/2}[(1 + \alpha_x)\cos\theta + \alpha_y\sin\theta] + \gamma E_0 + \gamma E_1 + 2\gamma\alpha_x E_0 \ .$$

By virtue of Eq. (1), we obtain

$$Q = 2\gamma(E_0E_1)^{1/2}[(1 + \alpha_x)\cos\theta + \alpha_y\sin\theta] + (1 - \gamma)E_0 - 2\gamma\alpha_x E_0 - (1 + \gamma)E_1 \ . \quad \text{(A3)}$$

Equation (A3) reduces to Eq. (2) if $(\alpha_x, \alpha_y) = (0, 0)$.

$Q(E_1, \alpha_x, \alpha_y)$ is now assumed to be constant within the range of α_x and α_y, and by differentiation, we find the variation

$$\Delta E_1 = -\left[\alpha_x\left(\frac{\partial Q}{\partial \alpha_x}\right) + \alpha_y\left(\frac{\partial Q}{\partial \alpha_y}\right)\right]\left(\frac{\partial Q}{\partial E_1}\right)^{-1} \ . \quad \text{(A4)}$$

From Eq. (2), which in our data treatment is used to transform measured energy spectra (E_1) into Q spectra, we find

$$\Delta Q = \frac{\partial Q}{\partial E_1}\ \Delta E_1 \ ,$$

which, by substitution into Eq. (A4), gives

$$\Delta Q_T = \overline{\alpha_x}\left(\frac{\partial Q}{\partial \alpha_x}\right) + \alpha_y\left(\frac{\partial Q}{\partial \alpha_y}\right),$$

and, by squaring, accordingly

$$\delta Q_T^2 = \overline{\alpha_x^2}\left(\frac{\partial Q}{\partial \alpha_x}\right)^2 + \overline{\alpha_x^2}\left(\frac{\partial Q}{\partial \alpha_y}\right)^2 \ , \quad \text{(A5)}$$

where δQ_T is the broadening of Q lines due to thermal target motion. The projections of the thermal target momentum $P_{x,T} = \alpha_x P_0$ and $P_{y,T} = \alpha_y P_0$ are independent stochastic variables, which are Gaussian distributed. The half-widths at $1/e$ height are $\sigma_{x,T} = \sigma_{y,T} = (2M_2kT)^{1/2}$, where k is the Boltzmann constant and T the absolute temperature of the target gas.

Accordingly, for both α_x and α_y, we find

$$\overline{\alpha_x^2} = \overline{\alpha_y^2} = kT/\gamma E_0 \ .$$

Insertion into Eq. (A5) gives

$$\delta Q_T^2 = \left[\left(\frac{\partial Q}{\partial \alpha_x}\right)^2 + \left(\frac{\partial Q}{\partial \alpha_y}\right)^2\right]\frac{kT}{\gamma E_0} \ , \quad \text{(A6)}$$

where δQ_T now is the half-width at $1/e$ height. $\partial Q/\partial \alpha_x$ and $\partial Q/\partial \alpha_y$ are calculated from Eq. (A3), and we finally get

$$\delta Q_T = 2\{kTE_0[1 - (E_1 + Q)/E_0]\}^{1/2} = 2(kTE_2)^{1/2} = 10(E_2)^{1/2}\ \text{eV}\ (E_2 \text{ in keV}) \ . \quad \text{(A7)}$$

2. *Recoil-Particle Method*

Starting from Eqs. (A1) and (A2) and eliminating θ, a straightforward calculation gives

$$Q = 2(E_0 E_2/\gamma)^{1/2}[(1+\alpha_x)\cos\phi - \alpha_y \sin\phi] - (1+1/\gamma)E_2 - 2\alpha_x E_0 , \quad \text{(A8)}$$

which, by setting $(\alpha_x, \alpha_y) = (0, 0)$, reduces to Eq. (3). The half-width at $1/e$ height is

$$\delta Q_T = 2\left(\frac{kTE_0[1-(E_2+Q)/E_0]}{\gamma}\right)^{1/2} = 2\left(\frac{kTE_1}{\gamma}\right)^{1/2} = 10(E_1/\gamma)^{1/2}\,\text{eV} \quad (E_1 \text{ in keV}). \quad \text{(A9)}$$

3. *Coincidence Method*

Kessel and Everhart[2] estimated the broadening effect of the thermal target motion in the case of $\gamma = 1$ only. An approximate calculation restricted to recoil-scattering angles in the neighborhood of 90° gives the more general result

$$\delta Q_T = 2[(kT/\gamma)E_0]^{1/2} = 10(E_0/\gamma)^{1/2}\,\text{eV} \quad (E_0 \text{ in keV}). \quad \text{(A10)}$$

A comparison of the three methods clearly shows that Q spectra obtained by the scattered-particle method are the ones least broadened by the thermal target motion. As $E_0 \simeq E_1$ for $\theta \ll 1$, it is noted that δQ_T in Eq. (A9) approximately equals δQ_T in Eq. (A10). As an example, let us consider 30-keV Al^+ on Ar, where $E_1 = 29.753$ keV, $E_2 = 0.127$ keV, and $Q_{II} = 0.120$ keV at scattering angle $\theta = 4°34'$. Then we obtain

scattered-particle method [Eq. (A7)]:

$\delta Q_T \sim 3.6$ eV ;

recoil-particle method [Eq. (A9)]:

$\delta Q_T \sim 67$ eV ;

coincidence method [Eq. (A10)]:

$\delta Q_T \sim 67$ eV .

Since $\bar{Q}_{II} - \bar{Q}_I$ is approximately 70 eV, the two peaks Q_I and Q_{II} will only be solved in Q spectra obtained by the scattered-particle method, where $2\delta Q_T \ll \bar{Q}_{II} - \bar{Q}_I$.

[1] V. V. Afrosimov, Yu. S. Gordeev, M. N. Panov, and N. V. Fedorenko, Zh. Tekhn. Fiz. 34, 1613 (1964); 34, 1624 (1964); 34, 1637 (1964); 36, 123 (1966) [Sov. Phys. Tech. Phys. 9, 1248 (1965); 9, 1256 (1965); 9, 1265 (1965); 11, 89 (1966)].

[2] Q. C. Kessel, A. Russek, and E. Everhart, Phys. Rev. Letters 14, 484 (1965); Q. C. Kessel and E. Everhart, Phys. Rev. 146, 16 (1966); E. Everhart and Q. C. Kessel, *ibid.* 146, 27 (1966).

[3] Q. C. Kessel, M. P. McCaughey, and E. Everhart, Phys. Rev. Letters 16, 1189 (1966); Phys. Rev. 153, 57 (1967).

[4] U. Fano and W. Lichten, Phys. Rev. Letters 14, 627 (1965).

[5] W. Lichten, Phys. Rev. 164, 131 (1967).

[6] V. V. Afrosimov, Yu. S. Gordeev, A. M. Polyanskii, and A. P. Shergin, Zh. Eksperim. i Teor. Fiz. 57, 806 (1969) [Sov. Phys. JETP 30, 441 (1970)].

[7] A. Russek and J. Meli, Physica 46, 222 (1970).

[8] C. Snoek, W. F. van der Weg, R. Geballe, and P. K. Rol, Physica 35, 1 (1967).

[9] Q. C. Kessel, in *The Fifth International Conference on the Physics of Electronic and Atomic Collisions, Leningrad*, 1967 (Leningrad Nauka Publishing, Leningrad, 1967), p. 92.

[10] F. W. Bingham, Phys. Rev. 182, 180 (1969).

[11] V. V. Afrosimov, Yu. S. Gordeev, A. M. Polyanskii, and A. P. Shergin, in *Proceedings of the Sixth International Conference on the Physics of Electronic and Atomic Collisions* (MIT Press, Boston, 1969), p. 744.

[12] E. J. Knystautas, Q. C. Kessel, R. Del Boca, and H. C. Hayden, Phys. Rev. A 1, 825 (1970).

[13] P. Loftager and G. Hermann, Phys. Rev. Letters 21, 1623 (1968).

[14] R. W. Fink, R. C. Jopson, H. Mark, and C. D. Swift, Rev. Mod. Phys. 38, 513 (1966).

[15] M. E. Rudd, T. Jorgensen, and D. J. Volz, Phys. Rev. 151, 28 (1966).

[16] C. Snoek, R. Geballe, W. F. van der Weg, P. K. Rol, and D. J. Bierman, Physica 31, 1553 (1965).

[17] G. N. Ogurtsov, I. P. Flaks, S. V. Avakyan, and N. V. Fedorenko, Zh. Eksperim. i Teor. Fiz. Pis'ma v Redaktsiyu 8, 541 (1968) [Sov. Phys. JETP Letters 8, 330 (1968)].

[18] T. A. Carlson and M. O. Krause, Phys. Rev. Letters 17, 1079 (1966).

[19] G. N. Ogurtsov, I. P. Flaks, and S. V. Avakyan, in *Proceedings of the Sixth International Conference on the Physics of Electronic and Atomic Collisions* (MIT Press, Boston, 1969), p. 274.

[20] G. M. Thomson, P. C. Laudieri, and E. Everhart, Phys. Rev. A 1, 1439 (1970).

[21] P. Dahl and D. C. Lorents (unpublished).

[22] B. Fastrup and G. Hermann, Phys. Rev. Letters 23, 157 (1969).

[23] G. H. Morgan and E. Everhart, Phys. Rev. 128, 667 (1962).

[24] M. P. McCaughey, E. J. Knystautas, and E. Everhart, Phys. Rev. 175, 14 (1968).

[25] M. T. Robinson, ORNL Report No. ORNL-3493 (unpublished).

[26] P. Loftager and G. Claussen, in *Proceedings of the Sixth International Conference on the Physics of Electronic and Atomic Collisions* (MIT Press, Boston, 1969), p. 518.